Bright AIE Nanoparticles for Two-Photon Imaging and Localized Compound Therapy of Cancers

Ying Li, [1#] Rongbing Tang, [3,5#] Xiaoyan Liu, [2,5] Junyi Gong, [4] Zujin Zhao, [7] Zonghai Sheng, [6] Jiangjiang Zhang, [2] Xuanyu Li, [2] Guangle Niu, [4] Ryan T. K. Kwok, [4] Wenfu Zheng, [5*] Xingyu Jiang, [2*] Ben Zhong Tang [1,4,7*]

[1] Center for AIE Research, College of Materials Science and Engineering, Shenzhen University, Shenzhen 518060, China.

[2] Department of Biomedical Engineering, Southern University of Science and Technology, No. 1088 Xueyuan Rd, Nanshan District, Shenzhen 518055, China.

[3] School of Stomatology, Lanzhou University, 199 Donggang Western Rd, Lanzhou 730000, China.

[4] Department of Chemistry, Hong Kong Branch of Chinese National Engineering Research Center for Tissue Restoration and Reconstruction, The Hong Kong University of Science and Technology, Clear Water Bay, Kowloon, Hong Kong, China.

[5] GBA Research Innovation Institute for Nanotechnology, CAS Key Lab for Biological Effects of Nanomaterials and Nanosafety, National Center for NanoScience and Technology, BeiYiTiao, ZhongGuanCun, Beijing 100190, China.

[6] Paul C. Lauterbur Research Center for Biomedical Imaging, Shenzhen Key Laboratory of Ultrasound Imaging and Therapy, CAS key laboratory of health informatics, Institute of Biomedical and Health Engineering, Shenzhen Institute of Advanced Technology, Chinese Academy of Sciences, Shenzhen, 518055, China.

[7] State Key Laboratory of Luminescent Materials and Devices, Guangdong Provincial Key Laboratory of Luminescence from Molecular Aggregates, South China University of Technology, Guangzhou 510640, China.

ABSTRACT: Photodynamic therapy (PDT) is a non-invasive therapeutic strategy for cancer treatment but it always suffers from low reactive oxygen species (ROS) efficiency generated from traditional organic dyes owing to weak absorption in the optical transparent window of biological tissues and fluorescence quenching at a concentrated solution or in nanoparticles. Herein, we present cationic lipid-encapsulated aggregation-induced emission (AIE) nanoparticles (NPs) that have a high quantum yield (23%) and a maximum two-photon absorption (TPA) cross-section of 560 GM irradiated by near infrared light (800 nm). The AIE NPs can serve as imaging agents for spatiotemporal imaging of tumor tissues with a penetration depth up to 505 µm on mice melanoma model. Noteworthy, the AIE NPs can efficiently generate singlet oxygen ($^1O_2$) and highly toxic hydroxyl radicals ($\cdot$OH) upon 800 nm-light irradiation for photodynamic tumor ablation. In addition, the AIE NPs can be effectively cleared from the mouse body after the imaging and therapy. This study provides a new strategy to develop theranostic agent for cancer image-guided PDT with high brightness, superior photostability and high biosafety.

KEYWORDS: aggregation-induced emission • photodynamic therapy • two-photon fluorescence imaging • therapeutic safety

Introduction

Cancer is one of the most serious diseases that severely threats the health of human beings.[1] Chemotherapy is one of the conventional modalities for cancer therapy.[2] However, systemic administration of anti-tumor drugs usually suffers from severe side

effects on account of the low bioavailability and tumor-therapeutic specificity.[3] Nanomedicine provides the possibility of delivering drugs to tumors by active or passive strategies.[4-8] However, its toxicity, the biodistrubution, retention, and clearance in the body are usually unclear. Furthermore, the dynamic therapeutic effects of the nanodrugs need to be monitored in a facile way.[9] Fortunately, the appearance of fluorescent theranostic agents provides partial solution for these problems.

Photodynamic therapy (PDT), on the other hand, is a typical theranostic strategie with minimal invasiveness, good specificity and negligible drug resistance and it has served as an effective cancer-therapy modality with high spatiotemporal precision.[10-12] During the PDT of cancer, an optically excited photosensitizer (PS) transfers its excited energy to the surrounding oxygen molecules to generate reactive oxygen species (ROS) such as superoxide anion radicals ($\cdot O_2^-$), hydroxyl radicals ($\cdot OH$), hydrogen peroxide radicals (H_2O_2), and singlet oxygen ($^1O_2$), to induce cancer cell death.[13,14] However, traditional PS molecules such as porphyrins, BODIPY and methylent subject to low extinction coeffcients and quantum yields (Φ_F). Theses characteristics yield reduced ROS generation and poor penetration depth in tumor tissues and ineffective therapy.[15-17] Recently, two-photon fluorescence imaging (TPFI) has become popular in biomedical diagnosis and therapy, due to its advantages of longer-wavelength excitation, lower autofluorescence, less photobleaching, higher 3D resolution, and deep imaging in tissues.[13, 18] Molecules with donor (D)-acceptor (A) structures usually have two-photon activity,[19-21] however, most of the reported molecules only emit weak light due to the twisted intramolecular charge transfer effect.

Aggregation-induced emission luminogens (AIEgens) are ideal fluorescence materials for bioimaging due to their high brightness and high photostability.[22-25] More importantly, some AIEgens were found to exhibit aggregation-enhanced ROS generation property, suggesting their great potential in image-guided PDT for cancers.[19,26]

In this study, we encapsulated an AIEgen TPE-PTB with cationic lipid to form nanoparticles (AIE NPs), which exhibited robust near infrared-I (NIR-I) two-photon absorbtion, bright far-red emission, high quantum yield, and efficient $^1O_2$ and ·OH release. NIR-I (800 nm) two-photon fluorescence imaging showed that AIE NPs accumulated in tumor tissues, especially the tumor blood vessels on mice melanoma model. Moreover, the AIE NPs exhibited excellent two-photon fluorescence image-guided PDT with an appropriate clearance rate (Scheme 1), demonstrating their great potential as a powerful and safe theranostic agent for clinical cancer treatments.

RESULTS AND DISCUSSION

Synthesis and Characterization of AIE NPs. TPE-PTB (AIE) was synthesized according to the reported method in literature.[27] To endow TPE-PTB with better biocompatibility, water dispersity, and other properties, it was composited with 1,2-dioleoyl-sn-glycero-3-phosphoethanolamine (DOPE) and 1,2-dioleoyl-3-trimethylammonium-propane (DOTAP) to form TPE-PTB nanoparticles (AIE NPs). The amount of TPE-PTB in lipid-encapsulated AIE NPs was determined by the standard curve (Figure S1), and the AIE encapsulation concentration was referred to our previous method.[28,29]
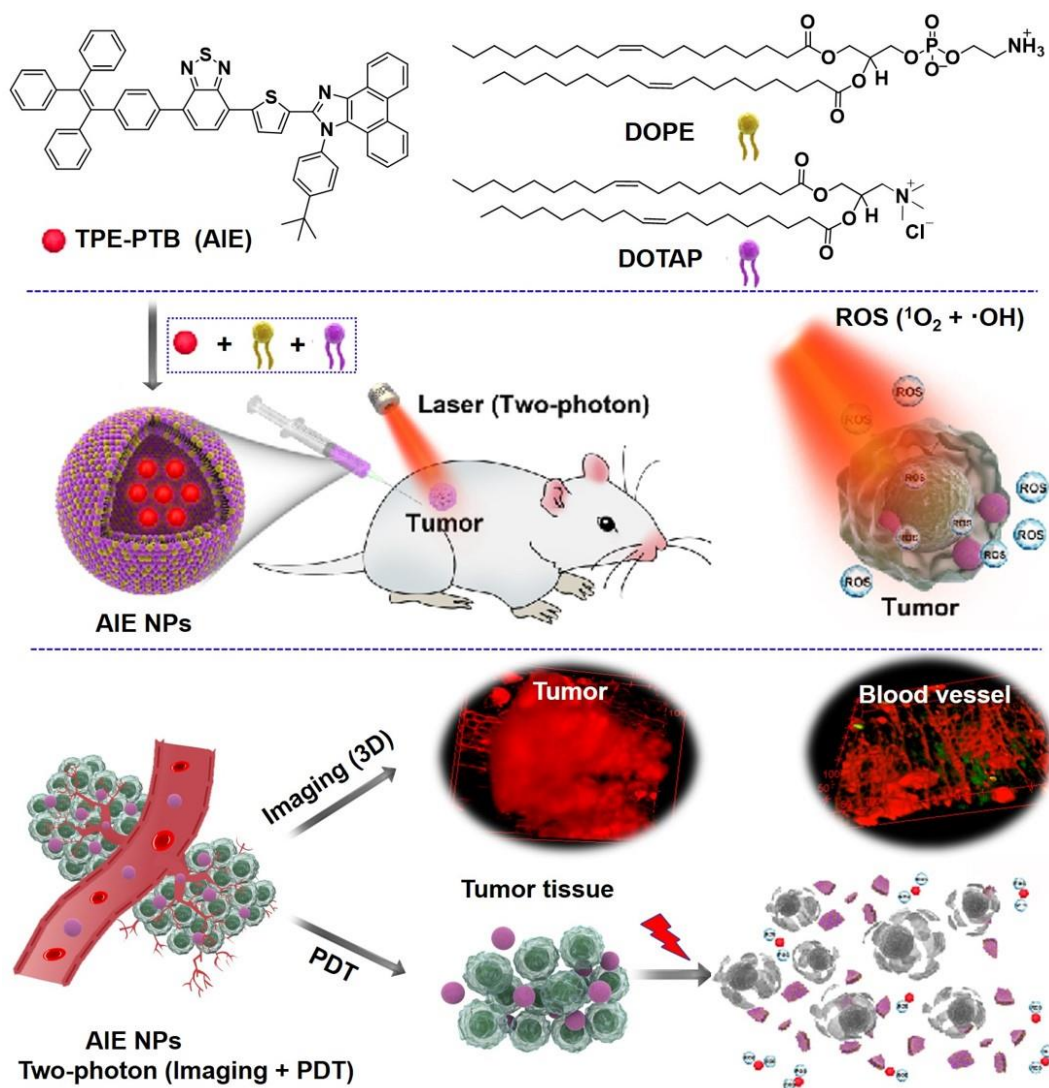
Scheme 1. Design and preparation of cationic lipid-encapsulated AIE NPs for two-photon fluorescence image (TPFI) and TPFI-guided PDT application.

We studied the morphology and photophysical property of AIE NPs. We used dynamic light scattering (DLS) to study the hydrodynamic diameter and size distribution of the AIE NPs which had an average hydrodynamic diameter of approximate 178 nm (polydispersity index of 0.15). Transmission electron microscopy (TEM) showed that the AIE NPs were spherical with a uniform diameter of approximate 160 nm (inset in Figure 1A). The different sizes of the AIE NPs reflected by TEM and DLS could be ascribed to the different measurement principles of the two methods.

TPE-PTB exhibited maximal absorption at 477 nm in chloroform whlie the absorption maxium of the AIE NPs in water was at 495 nm (Figure 1B). TPE-PTB in chloroform showed maximum fluorescence at 600 nm (Figure 1C), while AIE NPs in water had a fluorescence peak at 626 nm (Figure 1C). The red-shift of the photoluminescence (PL) peak should be accounted for the strong D-A interaction, and solvatochromic effects.[27] Moreover, the quantum yield (QY) of AIE NPs was as high as 23%, which could be ascribed to the strong D-A structure and effective π conjugation properties of the AIE molecule. Thus, we envisioned that the AIE NPs have two-photon absorption properties.[20,21] We measured the two-photon excitation spectra of TPE-PTB in chloroform and AIE NPs in water based on TPE-PTB concentration measured using Rhodamine 6G in methanol as a reference.[30] TPE-PTB and AIE NPs both had good two-photon absorption activities located at biological transparency window in the range of 700−880 nm. TPE-PTB in chloroform and AIE NPs in water showed intense PL peak at 601 nm and 632 nm, respectively under the NIR-I (800 nm) excitation (Figure S2). The emission of TPE-PTB in chloroform and AIE NPs in water showed no significant difference under one-photon and two-photon excitation. AIE NPs exhibited a two-photon absorption cross-section (δ) of 560 GM under NIR-I laser irradiation (800 nm) (Figure 1D). To further understand the different PL behaviors of TPE-PTB in chloroform and AIE NPs in water, two-photon confocal microscope was applied and the confocal images showed that the two-photon fluorescence lifetimes (FLIM) of TPE-PTB powder and AIE NPs powder were 3.1 ns and 3.9 ns, respectively (Figure S3), indicating that aggregation inhibited the nonradiative decay and prolonged the

1 fluorescence lifetime. Furthermore, the photothermal effect of AIE NPs was

2 investigated under continues two-photon laser exposure, setting phosphate buffered

3 saline (PBS) as a control. The temperature of PBS and AIE NPs solution increased from

4 25℃ to 27 ℃ after two-photon laser irradiaton for 13 min (Figure S4), demonstrating

5 that AIE NPs showed negligible thermal effect under two-photon irradiation.
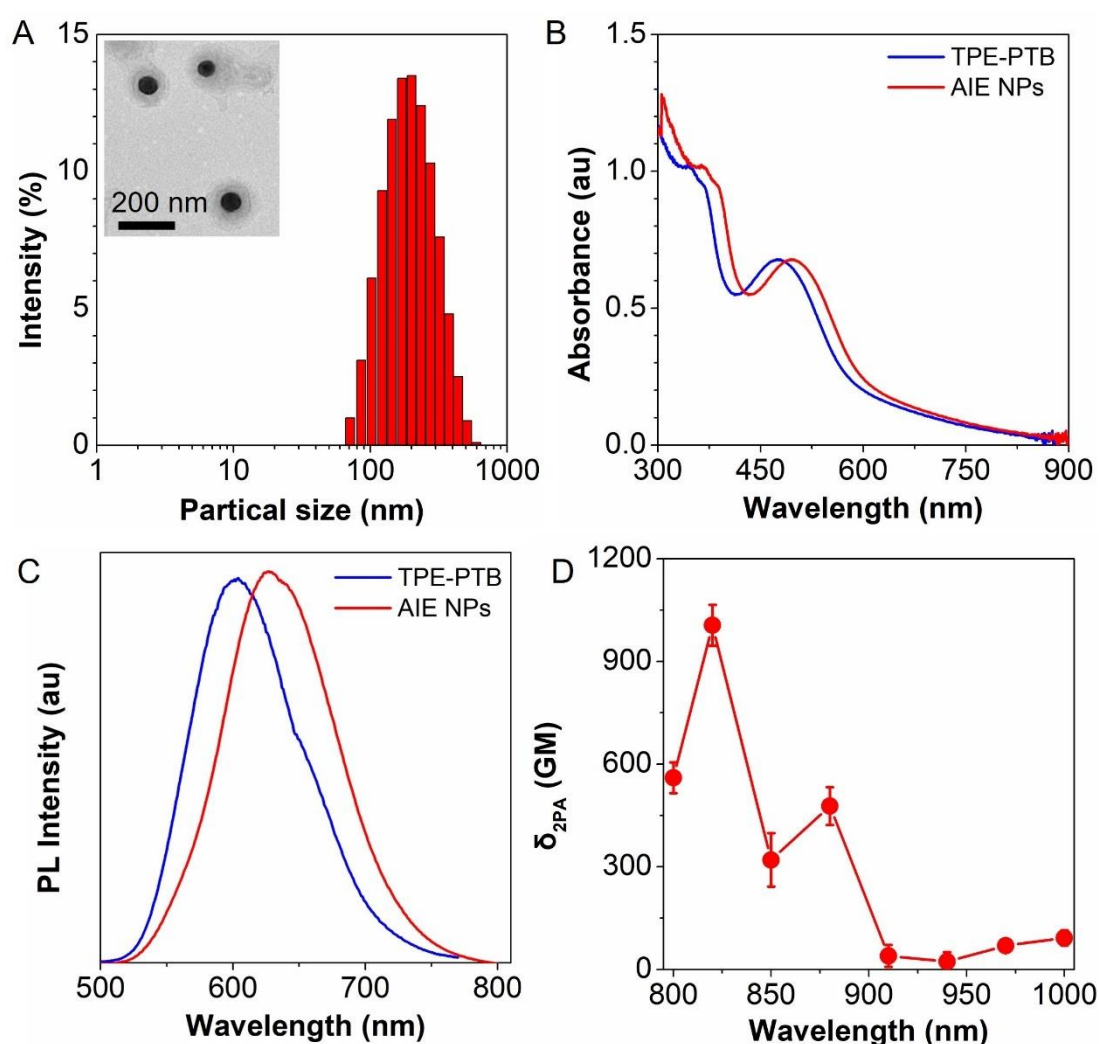
7 **Figure 1.** Characterization of AIE NPs. (A) DLS profile of AIE NPs. Inset: TEM image

8 of AIE NPs. (B) UV−vis absorption spectra of TPE-PTB in chloroform and AIE NPs in

9 water. (C) PL spectra of TPE-PTB in chloroform and AIE NPs in water (Ex = 488 nm).

10 (D) Two-photon absorption cross-section of AIE NPs in water.

11 **Singlet Oxygen Detection.** TPE-PTB is composed of a donor-acceptor (D-A) structure,

1   in which benzothiadiazole segment serves as an electron withdrawing moiety (A), while

2   1-phenyl-2-(thiophen-2-yl)-1H-phenanthro[9,10-*d*]imidazole segment functions as an

3   electron-donating moiety (D).[27] AIEgens with D-A characteristic have been

4   demonstrated to facilitate effective $^1O_2$ generation. [31,32] The ability of AIE NPs to

5   generate $^1O_2$ was evaluated by electron spin resonance (ESR) with 2,2,6,6-tetramethyl-

6   4-piperidinol (TEMP) as a commercialized singlet oxygen trapper.[33] Under white light

7   irradiation, the characteristic ESR signals of AIE NPs in aqueous solution showed a

8   large increase as compared to AIE NPs in darkness (Figure 2A). The $^1O_2$ generation

9   efficiency of AIE NPs in aqueous solution was further confirmed by 9,10-

10   anthracenediyl-bis(methylene)-dimalonic acid (ABDA) bleaching method. ABDA is a

11   commercialized probe used to quanifty $^1O_2$. Irradiated with white light, the absorbance

12   of ABDA at 378 nm decreased gradually in the presence of AIE NPs as a result of its

13   reaction with the generated $^1O_2$ (Figure 2B, Figure S5). The spin-orbit coupling matrix

14   elements (SOCMEs) were calculated using ORCA 4.1 in DFT method.[34,35] Big

15   SOCMEs were found between S3 to T9 and S8 to T9, with values of 1.01 cm^{-1} and 4.53

16   cm^{-1} (Figure 2C and Table S1). For a pure organic system, these SOCMEs indicated

17   that the intersystem crossing is able to take place after excitation. These results further

18   confirmed that AIE NPs can efficiently generate $^1O_2$ under white light irradiation.
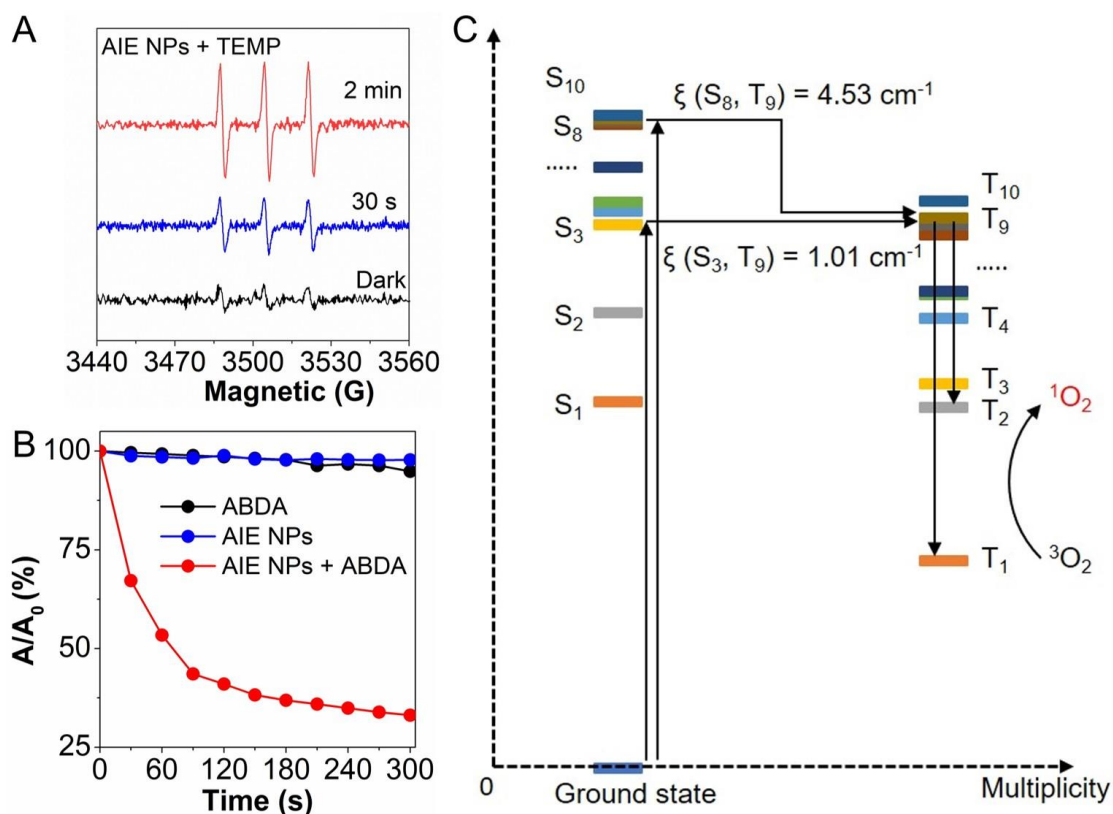
Figure 2. Light-induced singlet oxygen generation of AIE NPs. (A) ESR spectra from AIE NPs irradiated different time periods in the presence of TEMP before and after irradiation with a Xe arc lamp (171 mW cm^{-2}). (B) Plotting of relative absorbance of ABDA with light irradiation under different conditions, where A_0 and A are absorbances of ABDA at 378 nm. (C) Mechanism of singlet oxygen generation analysis.

Hydroxyl Radical Detection. We calculated the hydroxyl radical generation by quantum mechanism package ORCA 4.1.1[34,35] and proposed that AIE NPs could take one electron from environmental hydroxyl anion and change it to hydroxyl radical (Figure 3A). Thus, the compound would turn to an anion radical form. This proposed mechanism could be determined by calculating the Gibbs free energy of the whole process. The calculated Gibbs free energy equaled to -14.3839 kcal/mol, indicating a self-proposed reaction. Spin-trapping ESR is a powerful technique to detect the formation of $\cdot O_2^-$ and $\cdot OH$. We used 5,5-dimethyl-1-pyrroline N-oxide (DMPO) as

1   spin-trapping agent for both $\cdot O_2^-$ and $\cdot OH$.[36] White laser irradiation of AIE NPs and

2   DMPO led to the appearance of an ESR signal (Figure 3B), indicating the formation

3   of $\cdot O_2^-$ and $\cdot OH$. 3'-p-(Hydroxyphenyl) fluorescein (HPF), a specific probe for the

4   detection of hydroxyl radical, was used for further confirmation.[37] Irradiated with white

5   light, the absorbance of HPF at 523 nm increased gradually in the presence of AIE NPs

6   as a result of its reaction with the generated $\cdot OH$ (Figure 3C, Figure S6). The above

7   results indicate that AIE NPs can induce the formation of $\cdot O_2^-$ and $\cdot OH$ under white

8   light irradiation.

$$\Delta G^{\ominus} = -14.3839 \ kcal/mol$$
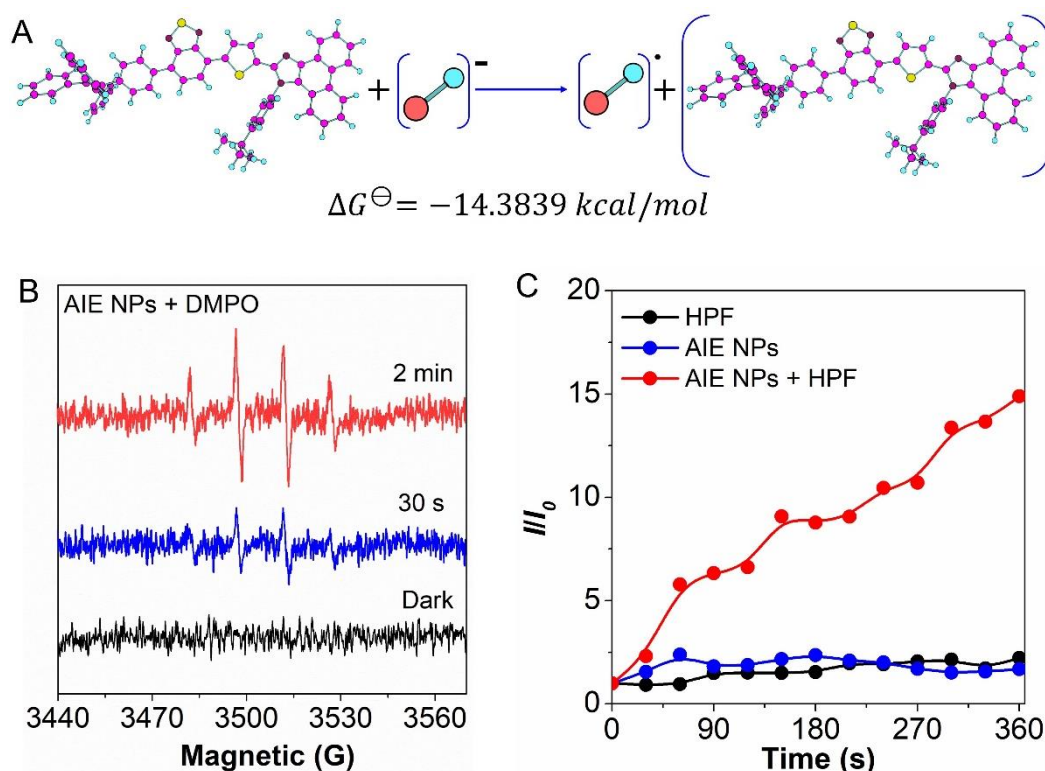
10   **Figure 3.** Light irradiation-induced hydroxyl radical generation of AIE NPs. (A)

11   Mechanism of hydroxyl radical generation analysis. (B) ESR spectra from AIE NPs

12   irradiated by different laser irradiation time periods in the presence of DMPO before

13   and after irradiation with a Xe arc lamp (171 mW cm^{-2}). (C) Plotting of relative PL

14   intensity (I/I_0) of HPF at 523 nm versus the irradiation time under light irradiation.

Cell Imaging, Photostability and Cellular Uptake of AIE NPs. We evaluated the

ability of AIE NPs under one-photon and two-photon bioimaging modes using confocal

laser scanning microscopy (CLSM) (Figure 4). The green fluorescence from one-

photon excitation were merged by the red fluorescence from two-photon excitation,

with the overlaid part showing yellow (Figure 4A). It is obvious that the two-photon

fluorescence images displayed the cells in more detailed than the one-photon

fluorescence images (Figure 4A), indicating that AIE NPs excited by two-photon can

exhibit the cell structure with a higher spatial resolution than that excited by one-photon

mode.

We observed the cellular uptake and distribution of AIE NPs by 2D and 3D CLSM

of the AIE NPs-treated A375 cells. Two-photon-excited fluorescence gave an imaging

depth of 14 μm (Z-stack of 14 slices, step size 1.0 of μm) (Figure S7A), while one-

photon-excited fluorescence imaging had a depth of 10 μm (Z-stack of 10 slices, step

size 1.0 of μm) (Figure S7B). By comparison, two-photon imaging mode exhibited

higher fluorescence intensity than that by one-photon mode (Figure S7). Furthermore,

3D fluorescence images revealed that the AIE NPs located inside the cells (Figure S7).

Lyso-tracker DR staining showed that AIE NPs colocalized with the lyso-tracker within

2 h and gradually sparated from the the lyso-tracker after 4 h in A375 cells (Figure S8),

indicating that AIE NPs entered the cells through the endosome-mediated endocytosis.

We tested the photostability of AIE NPs by continuous two-photon laser excitation and

sequential scanning with a confocal microscope (Figure 4B). Z-depth coding and

maximum intensity projection analysis method provided a visual map that tracks the

1 changes of fluorescence intensity of AIE NPs in A375 cells under continuous two-

2 photon laser irradiation at different time points (Figure 4C). The fluorescence signals

3 slightly decreased to ~75% of its initial values (Figure 4D, video in Figure S4) and the

4 morphology of the cells was still very clear after two-photon laser irradiation for 10

5 min. In comparison, , the fluorescence signals of lyso-rracker DR faded to 18% of its

6 initial values during the same process (Figure 4D). The high photostability of AIE NPs
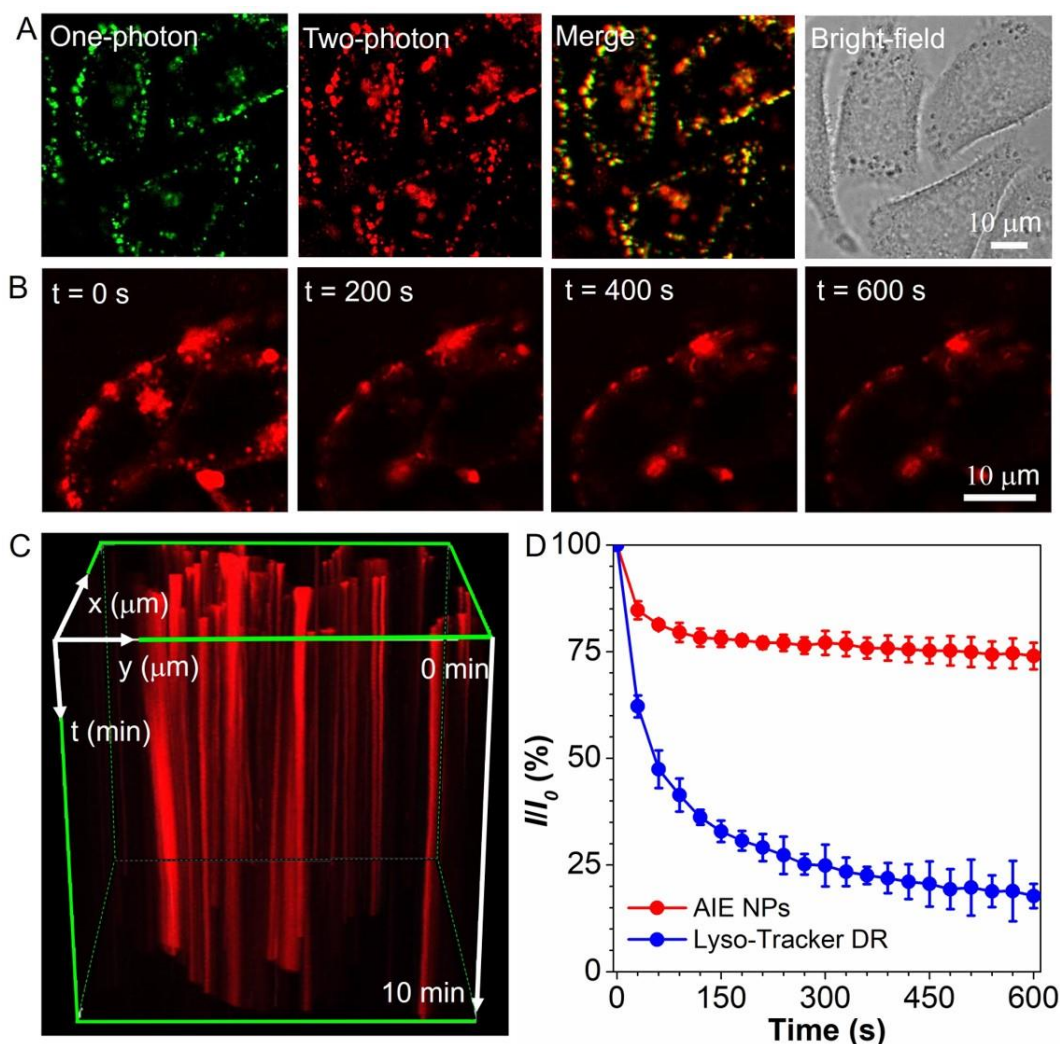
7 is favorable for in vivo imaging.

9 **Figure 4.** Cell imaging and photostability of AIE NPs. (A) One-photon and two-photon

10 imaging of A375 cells stained with AIE NPs (1 µg/mL) for 2 h. (B) Two-photon

11 imaging of AIE NPs in A375 cells under continuous two-photon laser irradiation (Ex =

800 nm, laser power = 2.0%). (C) Maximum intensity projection analysis the fluorescence intensity of A375 cells incubated by AIE NPs under continuous two-photon laser irradiation. (D) Photostability of AIE NPs and Lyso-tracker DR in A375 cells under two-photon laser continuous irradiation. Emission signal was normalized to the maximum intensity at the beginning of irradiation.

***Ex Vivo* Two-Photon Fluorescence Imaging.** We established melanoma model on mice by subcutaneously implantation of A375 cells in the abdomen and tested the imaging ability of AIE NPs with living melanoma tissues resected from tumor-bearing mice after intratumoral injection of AIE NPs at 2, 4 and 8 h, respectively. Under two-photon excitation, the paraffin section of tumor tissue with 5 µm thinckness had high intensity of fluorescence signal after 2 h injection, which did not show obvious change after 4 and 8 h (Figure 5A), indicating the high photostability of the AIE NPs. The tumor cells had higher fluorescence intensity than the other parts of the tumor tissue, and the fluorescence image can clearly show the tumor cell distribution in the tumor tissue (Figure S9). Surprisingly, the vascular network in the tumor tissue including the layer of blood vessel and red blood cells could be clearly displayed under the two-photon CLSM (Figure 5B). By comparison, two-photon excited fluorescence reached to a imaging depth of 74 µm (Z-stack of 75 slices, step size 1.0 of µm) while one-photon excited fluorescence imaging only had a depth of 20 µm (Z-stack of 26 slices, step size 0.8 of µm) (Figure 5C). Clearly, two-photon fluorescence mode is superior over one-photon mode in deep-tissue imaging. In addition, the 3D reconstructin of the fluorescence images revealed a homogenous distribution of AIE NPs in the tumor.
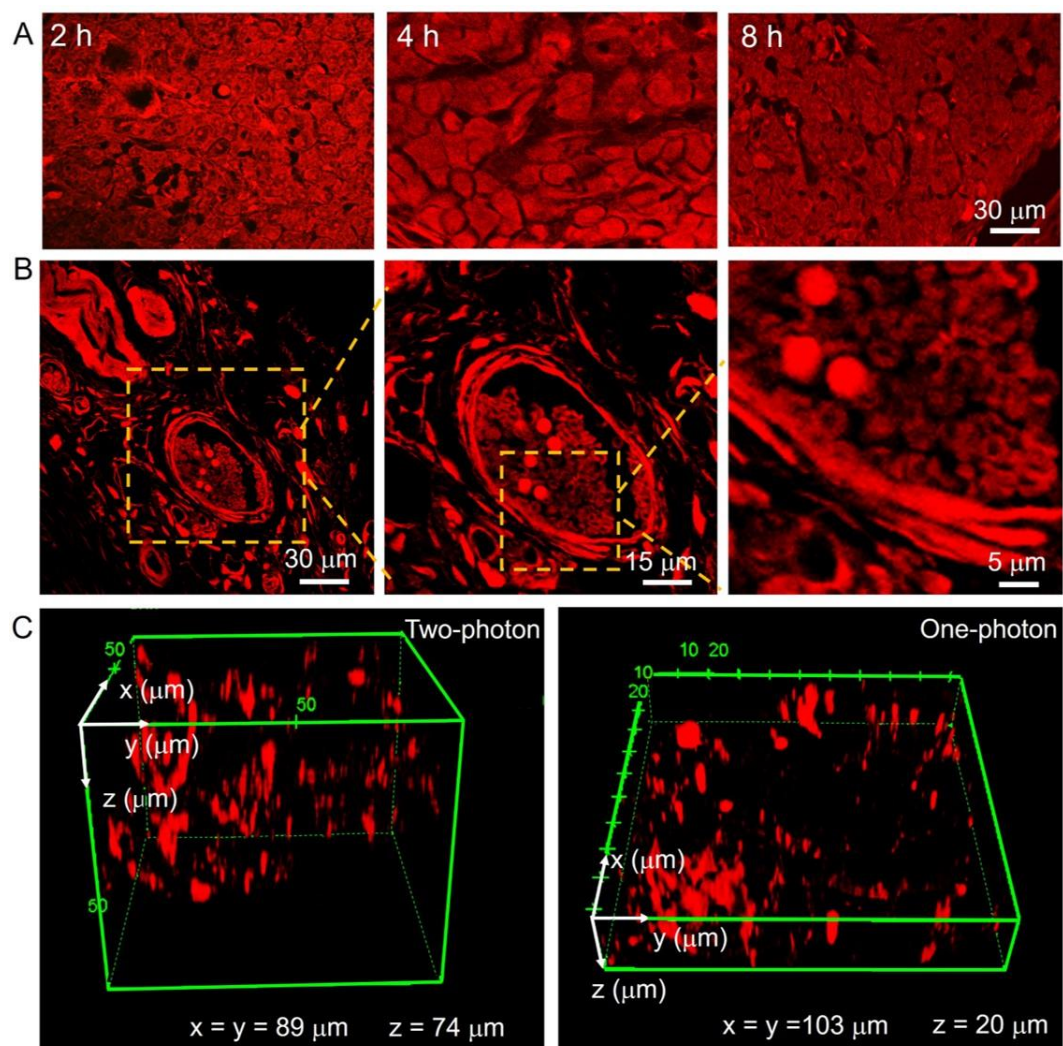
Figure 5. E*x vivo* two-photon images and 3D images of tumor biopsies. (A) Two-photon images of tumor biopsies. Tumor was removed after AIE NPs injected at 2, 4 and 8 h. (B) Two-photon images of tumor biopsies. Tumor was removed after AIE NPs injected at 4 h. The dotted yellow square indicated the magnified part of the images behind them. (C) Two-photon and one-photon *ex vivo* 3D reconstructed images along different axes of tumor tissue.

***In Vivo* Two-Photon Fluorescence Imaging.** We established a melanoma model on mouse ear to explore the application of AIE NPs in tumor vasculature imaging in vivo. Two considerations have been taken into account: one is that the tumor on the ear is convenient for observation under microscopy, another is that blood vessels play an

important role in the growth and metastasis of solid tumors.[38,39] The mouse ear tissue showed strong autofluorescence at 446 nm, which may come from the second harmonic generation (SHG) signals from collagen fiber in skin dermis.[40,41] However, the autofluorescence became weakened at 525 nm and no emission at 629 nm (Figure S10), indicating the imaging at or beyond 629 nm can avoid the interference of autofluorescence. After AIE NPs were injected into tumor, two-photon imaging of blood vessel at the boundary of tumor tissue were performed. Bright fluorescent signals from AIE NPs in the vascular network can be observed upon two-photon laser excitation at NIR-I (800 nm) (Figure 6A), indicating that AIE NPs had located in these structures within a short circulating time period. Strong SHG signals (green fluorescence) revealed that the tumor skin dermis has a thickness of around 80 μm (Figure S11). Most of the blood vessel networks and small blood capillaries can be visualized at various imaging depth from 0 to 50 μm, while major blood vessel network can still be observed from 60 to 80 μm upon two-photon laser excitation at 800 nm (Figure 6A). High contrast reconstructed 3D image clearly showed the blood vascular network located at the boundary of the tumor tissue (Figure 6B), where major blood vascular, small capillaries, and even deeply located arteries over 80 μm can also be clearly visualized, providing the spatiotemporal information of the whole vascular network.
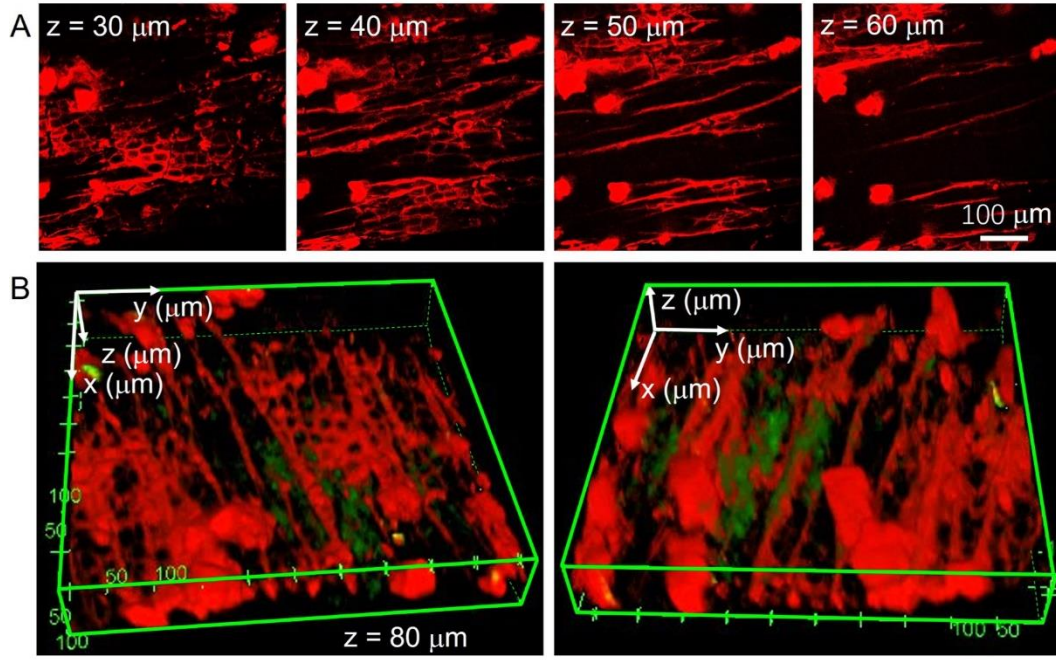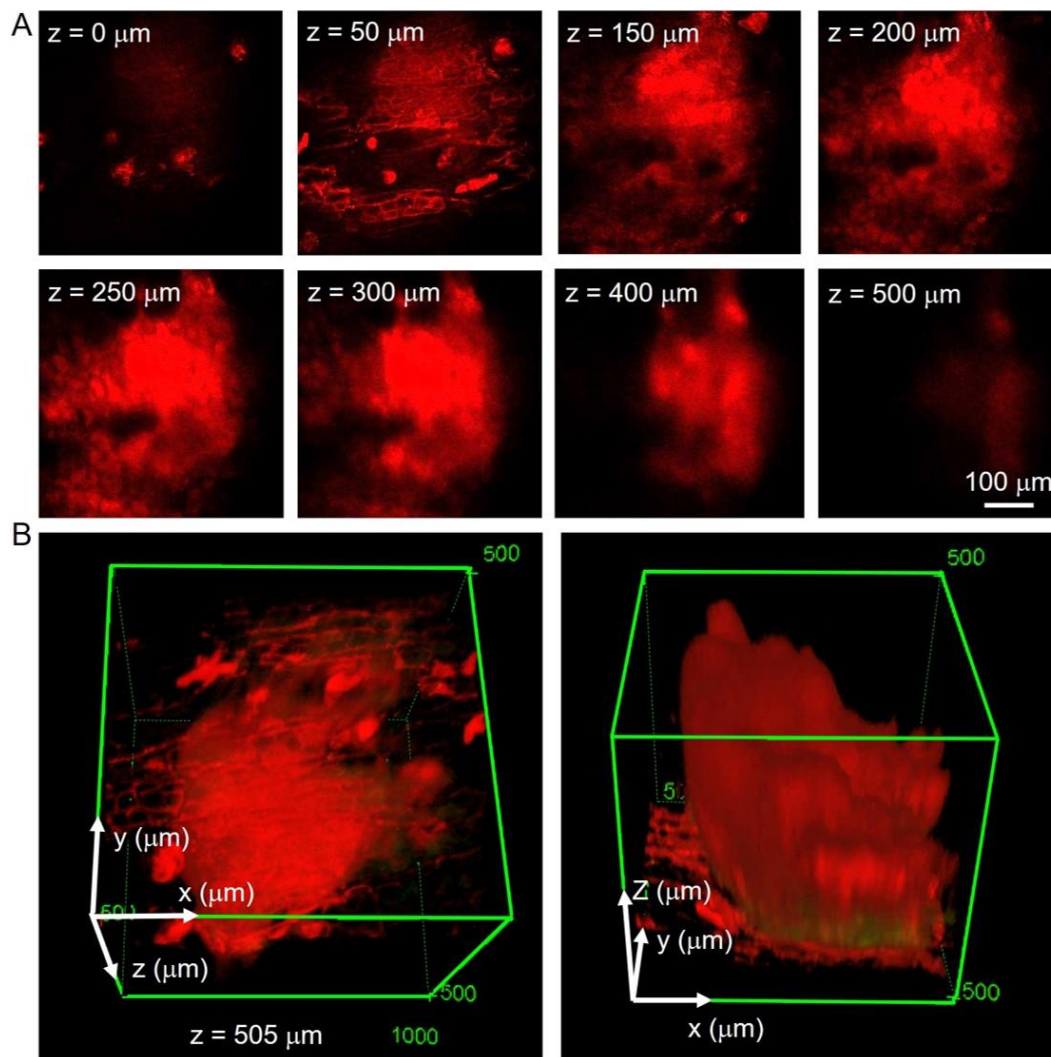
Figure 6. In *vivo* two-photon images at different vertical depth and 3D reconstruction of blood vessel near the tumor tissue after AIE NPs injection to the tumor for 30 min. (A) Z-projected images of blood vessel near the tumor tissue (Z-stack of 17 slices, step size of 5 μm, and imaging depth of 80 μm). (B) Two-photon 3D reconstructed images along different axes of tumor tissue from different surfaces. Ex = 800 nm, Em = 446 nm (green channel, laser power = 3.0 %) and Em = 629 nm (red channel, laser power = 3.0 %).

We examined the capability of AIE NPs for large depth imaging of tumor tissues *in vivo* under 800 nm laser excitation (Figure 7). Upon laser excitation, the two-photon fluorescence images at various depths of the same tumor from 0 to 500 μm were obtained. The detail structure of the tumor tissue was displayed clearly (Figure 7A, Figure S12), demonstrating the advantages of NIR-I excited AIE NPs for deep-tissue imaging. Reconstructed 3D image can clearly show the shape of the whole tumor and the inner structures such as vascular networks (Figure 7B, Figure S13). This result demonstrates NIR-I excited AIE NPs can provide high-resolution imaging for

vascular network inside or outside tumor tissues and tumor tissues with deep depth.

Figure 7. *In vivo* two-photon images at different vertical depth and 3D reconstruction of tumor tissue after AIE NPs injected to the tumor for 30 min. (A) Z-projected images of tumor tissue (Z-stack of 102 slices, step size of 5 μm, and imaging depth of 505 μm). (B) Two-photon 3D reconstructed images along different axes of tumor tissue from different surfaces. Ex = 800 nm, Em = 446 nm (green channel, laser power = 2.6 %) and Em = 629 nm (red channel, laser power = 2.6 %).

In Vitro Cytotoxicity. We evaluated the cytotoxicity of the AIE NPs using 3-(4,5-dimethyl-2-thiazolyl)-2,5-diphenyl-2-H-tetrazolium bromide (MTT) assay by incubating different concentrations of AIE NPs with A375 cells for 24 h without laser

irradiation. Over 90% of the cells were alive within 24 h even at concentration up to 5 μg/mL (Figure S14), indicating good biocompatibility of the AIE NPs.

Intracellular ROS Detection and PDT Efficiency of AIE NPs. We evaluated the intracellular ROS generation ability of AIE NPs in A375 cells with or without one-photon laser irradiation using 2′, 7′-dichlorodi-hydrofluorescein diacetrate (DCFH-DA) as a ROS fluorescence indicator. The AIE NPs-treated cells showed red fluorescence of the AIE NPs (Figure S15) and green fluorescence of DCFH-DA (Figure S16) with laser irradiation, while the control cells without AIE NPs incubation only showed weak fluorescence signal from DCFH-DA (Figure S16). After laser irradiation for 15 min, the control cells had no obvious morphological change (Figure S17), whereas the cells treated by AIE NPs showed nucleus shrinkage, leaking out of cytosol, and destruction of cytoskeleton (Figure S18). Noteworthy, the fluorescence of the AIE NPs kept stable during the irradiation period (Figure S15), demonstrating their superior photostability.

We compared the effects of one-photon and two-photon laser irradiation on viability of A375 cells. Two-photon laser irradiation brought higher cell damage than for one-photon irradiation (Figure S19), suggesting more ROS are generated. Without AIE NPs treatment, both one-photon and two-photon laser irradiation were safe to the cell in the same condition (Figure S20).

To further quantitatively confirm the intracellular ROS generation under NIR-I excitation, flow cytometry analysis using DCFH-DA as ROS indicator was conducted on A375 cells (Figure 8). The AIE NPs-treated cells without laser irradiation had a similar fluorescence signal as that of the control group. By contrast, the cells treated by

AIE NPs with laser irradiation (5 min) showed much higher fluorescence signal comparing with the cells without AIE NPs treatment at the same experimental condition (Figure 8 A, B). To evaluate the localized PDT effects of AIE NPs, A375 cells were stained with a Live (Calcein-AM)/Dead (Propidium Iodide, PI) viability/cytotoxicity kit, by which the living cells will show green fluorescence while the dead cells will show red fluorescence. Almost no living cells treated by AIE NPs could be observed within the laser irradiation area. On the contrary, almost all the AIE NPs-treated cells outside the laser irradiation area showed green fluorescence, indicating the controllable PDT therapy by localizing the irradiation area (Figure 8C). We used flow cytometry to quantitatively analyze PDT efficiency after stainning A375 cells with PI. More than 98% of AIE NPs-treated cells without laser irradiation remained alive (Figure 8D, E). By contrast, under laser irradiation, near 90% of the AIE NPs-treated cells were died (Figure 8 D, E). These results clearly demonstrated that AIE NPs had excellent PDT efficiency.
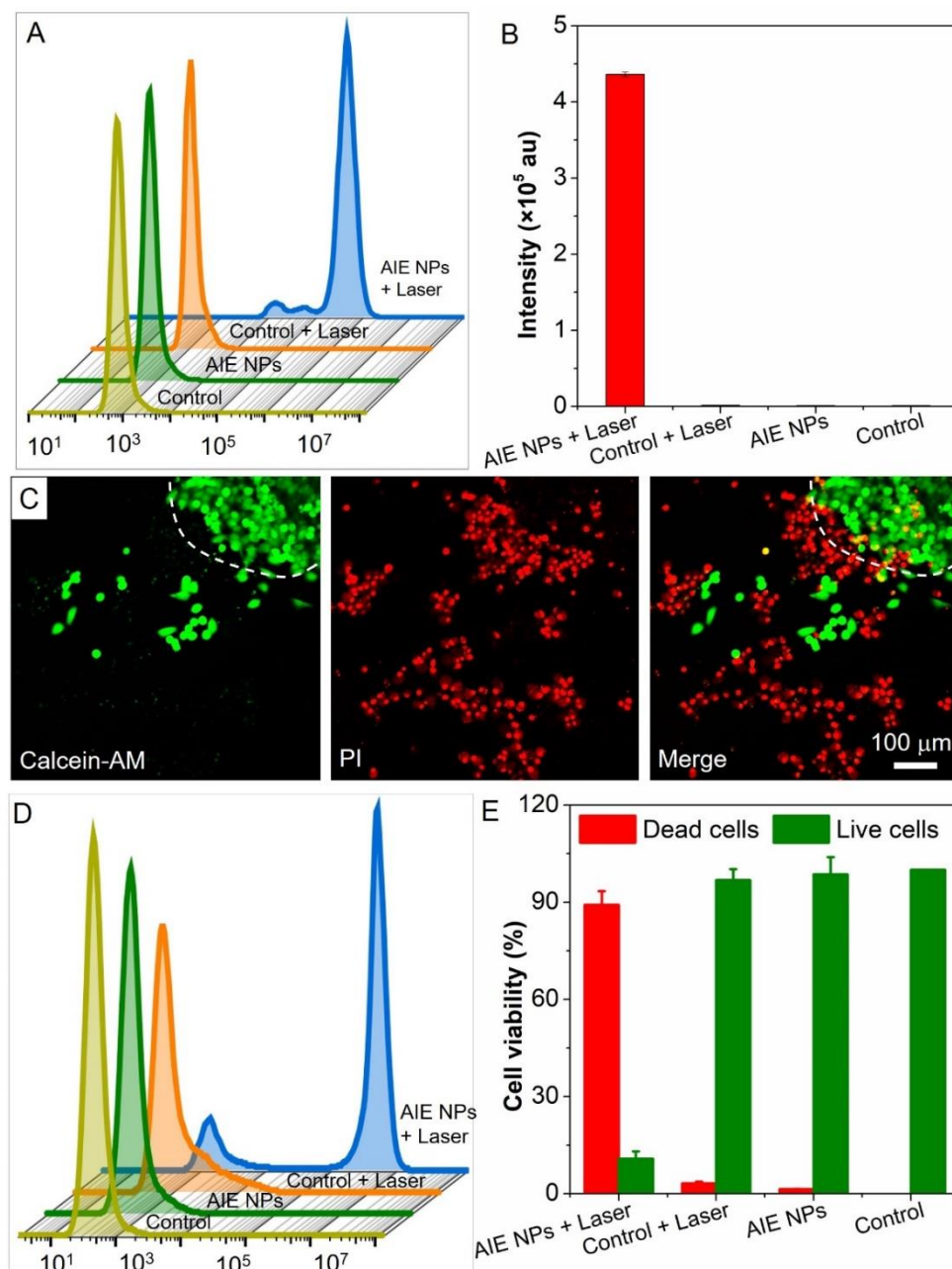
Figure 8. In *vitro* PDT killing A375 cells. (A, B) Average fluorescence intensity of intracellular ROS by flow cytometer after A375 cells treated with or without AIE NPs before and after two-photon laser irradiation for 5 min. (C) Fluorescence images of A375 cells stained with Calcein-AM/PI after incubated with AIE NPs (2 µg/mL, 2 h) and two-photon laser irradiation (450 mW/cm^2, 5 min) (Calcein-AM: Ex =488 nm , Em = 515 nm; PI: Ex = 541 nm, Em = 617 nm). (D, E) Flow cytometry of PI stained A375 cells after treated with and without AIE NPs before and after two-photon laser irradiation (450 mW/cm^2, 5 min).

In Vivo **Compound Photodynamic Therapy and Biosafety Evaluation**. We evaluated the antitumor efficacy of the AIE NPs *in vivo* on melanoma-bearing mice. Surprisingly, when we administrated AIE NPs by intravenous injection, fluorescence imaging showed that the NPs still retained in the mice tail veins after 1 h of injection (Figure S21), reflecting that AIE NPs have excellent retention capability which is an advantage for maintaining high therapeutic concentration in a localized area. This property may be ascribed to the positively charged surface of the NPs, which may facilitate the binding if the NPs with negatively charged cell surface. We thus used intratumoral injection method to exploit this merit of the AIE NPs in the followed experiments. To avoid the possible thermotherapy effects during the PDT therapy, the tumor temperature in mice injected with PBS (the control) and AIE NPs were controlled below 40°C after continuous irradiation (Ex = 800 nm, 450 m W/cm^2, 10 min) (Figure S22). The tumor-bearing mice treated by PBS with or without laser irradiation showed rapid tumor growth (Figure 9A, B). By contrast, the AIE NPs-treated mice with laser irradiation showed remarkable inhibition of tumor growth (Figure 9A, B). These results were further confirmed by hematoxylin and eosin (H&E) staining after the PDT. The tumor cells in mice treated by PBS with or without laser irradiation still retained their normal morphology with distinguishable membrane and nuclear structures. Similarly, the tumor treated with AIE NPs without laser irradiation also showed no obvious cellular and tissue damage (Figure 9C). By contrast, AIE NPs-treated mice with laser irradiation showed significant cellular and tissue damage, as indicated by cytoplasmic efflux, nuclear shrinkage, and tissue cavitation (Figure 9C). The mice treated with AIE

NPs with or without laser irralidation had no significant body weight loss (Figure S23), suggesting the low systematic toxicity of AIE NPs. The results were further confirmed by pathological assessments. There was no noticeable tissue damage in any of the major organs (heart, liver, spleen, lung and kidney) after the AIE NPs-mediated PDT compared with the control group (Figure S24). It is worth mentioning that in the PBS plus laser irradiation group, the tumor metastasized to the liver (Figure S24). Together, the above results clearly demonstrated that AIE NPs have excellent antitumoral capability with minimal side effects.
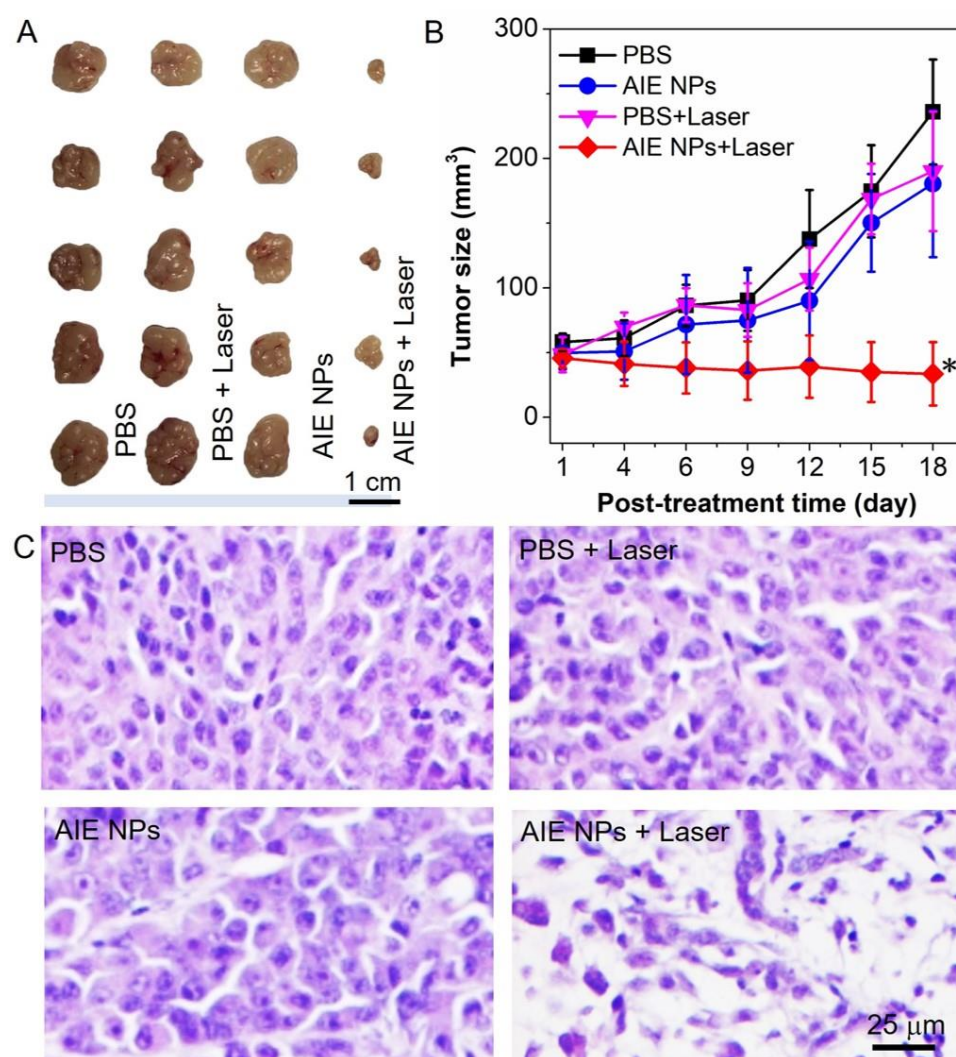
Figure 9. *In vivo* evaluation of AIE NPs in treatment of tumor-bearing mice after two-photon laser irradiation (800 nm, 450 mW/cm^2, 10 min). (A) Photograph of the resected

tumors in different treatment groups. (B) Tumor growth curve during the treatments as indicated (n=5). All date are presented as mean ± SD, *$P < 0.05$. (C) H&E staining images of tumor slices collected from mice 18 days post-treatments as indicated.

We studied if AIE NPs can be cleared from the body by observing the distribution of the NPs in mice after intratumoral injection. There was a strong fluorescence signal localized in the tumor cite after intratumor injection of AIE NPs for 1 h, and the fluorescence intensity gradually decreased with the increase of time (Figure 10A, B). There was no obvious fluorescence signal after 5 days, and the fluorescence intensity was similar to that of the control group (Figure 10B, Figure S25). The tumor and main organs were removed from the body for further analysis. Like the control group, the AIE NPs-treated group had no visible fluorescence signal day 5 post-injection (Figure 10C, Figure S26). Also, there was no AIE NPs fluorescence signal in the blood day 5 post-injection (Figure 10D). Together, these results clearly demonstrated that AIE NPs can be effectively cleared from the body with minimal side effects.
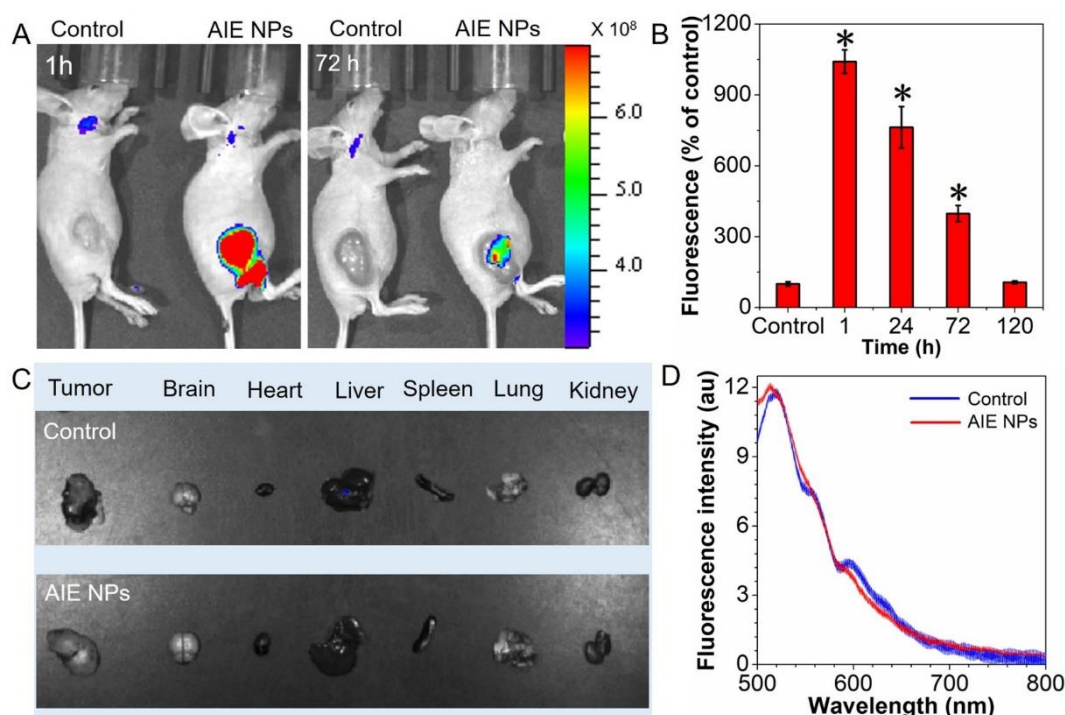
Figure 10. The clearance of AIE NPs *in vivo*. (A) The *in vivo* fluorescence images of the tumor-bearing mice taken at 1 and 24 h after intratumor injection of AIE NPs. (B) Relative fluorescence intensity of tumor in AIE NPs-treating group and the control group. (C) The *ex vivo* images of the tumor and major organ tissues of tumor-bearing mice 120 h post-injection with or without AIE NPs. (D) The fluorescence intensity of AIE NPs in mice blood 120 h post-injection (Ex = 488 nm, Em = 500-800 nm).

CONCLUSION

In this study, we developed cationic lipid-encapsulated AIE NPs for two-photon fluorescence-guided photodynamic therapy. The AIE NPs, which had a maximum two-photon absorption cross-section (δ) of 560 GM at NIR-I (800 nm) and a quantum yield of 23%, showed the capability to imaging deep (up to 505 nm) tumor tissues spatiotemporal with high-resolution. Noteworthy, the AIE NPs can generate both singlet oxygen ($^1O_2$) and hydroxyl radicals ($\cdot$OH) for enhanced photodynamic therapy. Besides, AIE NPs can be retained locally and cleared effectively, demonstrating an

excellent property for high therapeutic efficacy and high biosafety. The AIE NPs are promising as a theranostic agent for biomedical applications.

EXPERIMENTAL SECTION

Chemicals and Methods. All the chemicals and reagents were purchased from Sigma-Aldrich or Acros. The TPE-PTB fluorogen was prepared following our previously published protocol.[27] Milli-Q water was from a Milli-Q purification system (Merck Millipore, Germany). Steady-state photoluminescence (PL) spectra were conducted on a Perkin-Elmer spectrofluorometer LS 55. The absolute fluorescence quantum yield was measured using a Hamamatsu quantum yield spectrometer C11347 Quantaurus_QY. The fluorescence lifetime was measured using a Hamamatsu Compact Fluorescence Lifetime Spectrometer C11367. Dynamic light scattering (DLS) and zeta potential was performed on a Zetasizer Nano ZS (Malvern Panalytical Corporation). Two-photon sprectra were measured on Tsunami-Spitfire-OPA-800C (Spectra-Physics). Transmission electron microscopy (TEM) images were acquired from a 120 KV-TEM (HT7700). Cell images were collected using a confocal laser scanning microscope (CLSM) (Zeiss710) and two-photon CLSM (Olympus FV1000). The temperature images were recorded on an infrared thermal camera (FLIR E40).

Synthesis and Characterization of the AIE NPs. 3 mL of chloroform solution containing 1,2-dioleoyl-sn-glycero-3-phosphoethanolamine (DOPE) (10 mg/mL, 100 μL), N-[1-(2,3-dioleoyloxy) propyl]-N,N,N-trimethylammonium methyl-sulfate (DOTAP) (10 mg/mL, 150 μL) and AIE (1 mg/mL, 50 μL) were poured into a round-bottomed flask, treated by thin film hydration on a rotary evaporator (37°C, 100 rpm)

1 (Heidolph Hei-VAP Value Digital) for 20 min, and the film was kept rest overnight

2 before resuspended in water followed by an sonication to form liposome. Diameter,

3 polydispersed index (PDI) and zeta potential of the samples were recorded by Zetasizer

4 Nano ZS.

5 **Determination of AIE Encapsulation Concentration.** The UV-Vis absorption

6 intensity of a series of AIE solutions in chloroform at 488 nm was measured.[28]The

7 standard curve of the AIE UV-Vis absorption intensity versus concentration was then

8 obtained (Figure S1). 1 mL of AIE NPs stock solution was freeze-dried and then

9 dissolved in 1 mL of chloroform, and then the UV-Vis absorption intensity at 488 nm

10 was obtained. The amount of AIE encapsulated in AIE NPs was determined from the

11 standard curve.

12 **Singlet Oxygen Detection.** Singlet oxygen generated by photoirradiation of AIE NPs

13 in water was detected by using electron spin resonance technique (Bruker EMXplus-

14 10/12, Bruker) in the presence of 160×10^{-3} M 2,2,6,6-tetramethyl-4-piperidinol

15 (TEMP). The EPR signals of the free radical TEMPO (g = 2.0060, a_N = 17.3 G)

16 generated by the reaction of singlet oxygen with TEMP were recorded before and after

17 irradiation by a Xe arc lamp (LSB530A, obtained from LOT-Quantum Design GmbH)

18 with a spectral range of 200-900 nm (171 mW cm^{-2}). The singlet oxygen generated

19 from the AIEgens in water upon white light irradiation was also studied by using ABDA

20 as an indicator. The absorbance of ABDA (50 μM) at 378 nm was recorded at different

21 irradiation times to obtain the decay rate of the photosensitizing process.

22 **Hydroxyl Radical Detection.** Hydroxyl radical generated by photoirradiation of AIE

NPs in water was detected by electron spin resonance technique in the presence of DMPO ((Dojindo, Japan). The hydroxyl radical generated from the AIEgens (6 µg/mL) in water upon Xe arc lamp white light irradiation was also studied by using HPF as an indicator. The absorbance of HPF (33 µM) at 523 nm was recorded at different irradiation times to obtain the decay rate of the photosensitizing process.

Cell Culture. A375 cells were purchased from ATCC and cultured in Dulbecco's modified eagle medium (DMEM) with 1% penicillin G (P) (100 U mL^{-1}) and streptomycin (S) (100 U mL^{-1}) and 10% fetal bovine serum (FBS) at 37°C in a humidified incubator with 5% CO$_2$. The culture medium was changed every three days and the cells were collected by treating with 0.25% trypsin-EDTA solution after they reached confluence.

Cell Imaging. A375 cells (4 × 10^4 cells mL^{-1}) were seeded in confocal dish. After 24 h culture, cells were stained with AIE NPs (1 µg/mL) for 2 h. Before imaging on the confocal fluorescence microscope (ARsiMP-LSM-Kit-Legend Elite-USX), the cells were washed with PBS three times.

Cell Viability Assay. A375 cells were seeded in 96-well plates (1 × 10^4 cells 200 µL^{-1}) and incubated for 24 h. The medium was removed and AIE NPs was added at different concentrations (0, 0.625, 1.25, 2.5, 5 µg/mL) and incubated in darkness for 24 h. 100 µL of fresh medium containing 10 µL MTT solution was added into each well after the removal of the culture medium, and the cells were incubated at 37°C for 3-4 h. 100 µL DMSO was added after the removal of the MTT medium. The absorption of the samples was measured on a microplate reader (Tecan, infinite M200, Switzerland) at 570 nm.

1   The results were analyzed by Origin Pro 8.0.

2   **Animal Model.** BALB/C nude mice (6 weeks, female) (Beijing Vital River Laboratory

3   Animal Technology Co. Ltd., China) were used in the *in vivo* experiments. All

4   procedures involving animal use were approved by the Institutional Animal Care and

5   Use Committee of Institute of Process Engineering, Chinese Academy of Sciences. To

6   establish the xenograft A375 tumor-bearing mouse model, 3×10^6 cells suspended in 200

7   µL DMEM medium were injected subcutaneously into the mouse. When the tumor

8   volumes reached about 40-60 mm^3, the animals were used subsequently.

9   *In Vivo* **Tumor and Blood Vessel Imaging**. To establish a melanoma subcutaneous

10   xenotransplanted tumor model, A375 cells (1×10^6 cells in 40 µL of PBS) were

11   subcutaneously injected in the mice ear root. Tumor-bearing mice were used for the

12   experiments when the tumor volume reached 30-50 mm^3. Animal experiments were

13   carried out under the protocol approved by Shenzhen Institutes of Advanced

14   Technology, Chinese Academy of Sciences Animal Care and Use Committee.

15   Intratumoral injection dose was 25 µL (4 µg/mL), while intravenous dose was 50 µL

16   (4 µg/mL).

17   Two-photo fluorescence imaging was carried out with a two-photon confocal

18   microscope (Nikon A1 plus, 25x water objective, working distance (WD) = 2 mm,

19   numerical aperture (NA) = 1.1, Excitation wavelength = 800 nm, Emission wavelength

20   = 635 nm).

21   **Intracellular ROS Detection and Cell Death Measurement.** A375 cells were seeded

22   in confocal plates for 24 h. A375 cells were incubated with total reactive oxygen

species (ROS) assay kit for 0.5 h at 37 °C in the dark after AIE NPs (2 µg/mL) added

for 2 h. The cells were then harvested and washed three times with phosphate buffer

saline (PBS). The fluorescence intensity was measured using a CLSM, with one-

photon (488 nm) excitation.

To measure the levels of intracellular ROS, the treated cells were incubated with

ROS assay kit for 0.5 h at 37 °C in the dark. The cells were then harvested and washed

three times with PBS. The fluorescence intensity was measured using a flow

cytometer (Cell Lab Quanta SC, Beckman, USA) with two-photon excitation

(800 nm).

Dead cells were detected using a propidium iodide (PI) dye (Invitrogen^{TM},

Thermo Fisher Scientific). A375 cells were seeded in culture dishes with a diameter

of 6 cm and then subjected to indicated treatments. The cells were then collected,

washed with PBS twice. PI was added and mixed after the cells treated by two-photon

irradiation, and the cells were incubated for 10 min at room temperature in darkness.

Finally, the cells were analyzed using a flow cytometer (Cell Lab Quanta SC,

Beckman, USA) with an excitation wavelength of 543 nm after the cells washed with

PBS twice.

***In Vitro and In Vivo* Photothermal Imaging.** The temperature changes of the PBS,

AIE NPs (4 µg/mL) in solution or PBS-, AIE NPs-treated tumors under 800 nm two-

photon laser irradiation (450 mW cm^{-2}) were monitored every 1 min through an infrared

thermal camera (FLIR E40).

***In Vivo* Photodynamic Therapy.** The xenograft A375 tumor-bearing mice were

randomly divided into four groups (with or without laser irradiation.), and every group had five parallel samples (n = 5). PBS, AIE NPs（4 µg/mL based on TPE-PTB, 50 µL）were injected into the tumor, respectively. After injection 2 h, the tumors of mice (2 groups) were continuously irradiated with two-photon laser for 10 min (800 nm, 450 mW/cm^2). The mouse body weight and the tumor volumes were measured every 2 or 3 days after a variety treatments. The tumor volume was calculated according to the following formula: Volume = Width^2 × Length/2.[42]

Histological Analysis. Histological analysis of the wounds was carried out on day 18 post-treatment. The heart, liver, spleen, lung, kidney and tumor were collected and fixed in 4% formaldehyde solution, and the pathological sections of tumor tissues were analyzed by Hematoxylin and Eosin (HE) staining. Histological images were taken using an inverted microscope (Olympus, IX71, Japan).

In vivo **Imaging of Tumor-bearing Mice.** The xenograft A375 tumor-bearing mice were randomly selected for fluorescence imaging experiments. The tumor-bearing mice (n = 3 mice) were anesthetized using 2% isoflurane in oxygen, and AIE NPs (4 µg/mL, 50 µL) were intratumor injected into the tumor-bearing mice using a microsyringe. In vivo fluorescence imaging was performed with Maestro EX fluorescence imaging system (CRi, Inc.). The light with a central wavelength at 488 nm was selected as the excitation, and fluorescence signal in the spectral region of 600-750 nm was collected. The main organ and tumor fluorescence also measured 5 days post-injection.

Statistical Analysis. The values reported were expressed as mean standard deviation (SD). The Origin 8 software was used for graph plotting. A value of $P < 0.05$ was

considered significant. Each experiment included at least three replicates.

Author Contributions

Y. L and R. B. T. contributed equally to this work.

Notes

The authors declare no competing financial interest.

REFERENCES

(1) Lin, H.; Chen, Y.; Shi, J. L. Nanoparticle-triggered in situ catalytic chemical reactions for tumour-specific therapy. *Chem. Soc. Rev*. **2018**, *47*, 1938-1958.

(2) Yuan, Z. F.; Zhao, D.; Yi, X. Q.; Zhuo R. X.; Li, F. Steric Protected and Illumination-Activated Tumor Targeting Accessory for Endowing Drug-Delivery Systems with Tumor Selectivity. *Adv. Funct. Mater.* **2014**, *24*, 1799-1807.

(3) Huo, M. F.; Wang, L. Y.; Chen, Y.; Shi, J. L. Tumor-selective catalytic nanomedicine by nanocatalyst delivery. *Nat. Commu.* **2017**, *8*, 0.1038/s41467-017-00424-8.

(4)   Rodríguez-Nogales, C.; González-Fernández, Y.; Aldaz, A.; Couvreur, P.; Blanco-Prieto, M. J. Nanomedicines for Pediatric Cancers. *ACS Nano* **2018**, *12*, 7482-7496.

(5)   Wang, J.; Zhang, L.; Peng, F.; Shi, X.; Leong, D. T. Targeting Endothelial Cell Junctions with Negatively Charged Gold Nano-particles. *Chem. Mater*. **2018**, *30*, 3759-3767.

(6)   Torchilin, V. P.; Lukyanov, A. N.; Gao, Z. G.; Papahadjopoulos-Sternberg, B. Immunomicelles: targeted pharmaceutical carriers for poorly soluble drugs. *Proc. Natl. Acad. Sci.* USA. **2003**, *100*, 6039-6044.

(7)   Pan, L. M.; He, Q. J.; Liu, J. N.; Chen, Y.; Ma, M.; Zhang, L. L.; Shi, J. L. Nuclear-targeted drug delivery of tat peptide-conjugated monodisperse mesoporous silica nanoparticles. *J. Am. Chem. Soc.* **2012**, *134*, 5722-5725.

(8)   Dhar, S.; Gu, F. X.; Langer, R.; Farokhzad, O. C.; Lippard, S. J. Targeted delivery of cisplatin to prostate cancer cells by aptamer functionalized Pt(IV) prodrug-PLGA-PEG nanoparticles. *Proc. Natl. Acad. Sci. USA.* **2008**, *105*, 17356-17361.

(9)   Lee, E. S.; Gao, Z.; Bae, Y. H. *J. Control. Release* **2008**, *132*, 164-170.

(10) Li, J.; Pu, K. Development of Organic Semiconducting Materials for Deep-Tissue Optical Imaging, Phototherapy and Photoactivation. *Chem. Soc. Rev.* **2019**, *48*, 38-71.

(11) Cui, D.; Huang, J.; Zhen, X.; Li, J.; Jiang, Y.; Pu, K. A Semiconducting Polymer Nano-prodrug for Hypoxia-Activated Photodynamic Cancer Therapy. *Angew. Chem., Int. Ed.* **2019**, 58, 5920.

(12) Li, J.; Huang, J.; Lyu, Y.; Huang, J.; Jiang, Y.; Xie, C.; Pu, K. Photoactivatable Organic Semiconducting Pro-nanoenzymes. *J. Am. Chem. Soc*. **2019**, *141*, 4073-4079.

(13) Shen, Y. Z.; Shuhendler, A. J.; Ye, D. J.; Xu, J. J.; Chen, H-Y. Two-photon excitation nanoparticles for photodynamic therapy. *Chem. Soc. Rev.*, **2016**, *45*, 6725-6741.

(14) Wang, H.; Yang, X. Z.; Shao, W.; Chen, S. C.; Xie, J. F.; Zhang, X. D.; Wang, J.; Xie, Y. Ultrathin Black Phosphorus Nanosheets for Efficient Singlet Oxygen Generation. *J. Am. Chem. Soc.* **2015**, *137*, 11376-11382.

(15) Singh, S.; Aggarwal, A.; Bhupathiraju, N. V. S. D. K.; Arianna, G.; Tiwari, K.; Drain, C. M. Glycosylated Porphyrins, Phthalocyanines, and Other Porphyrinoids for Diagnostics and Therapeutics. *Chemical Reviews* **2015**, *115*, 10261-10306.

(16) Celli, J. P.; Spring, B. Q.; Rizvi, I.; Evans, C. L.; Samkoe, K. S.; Verma, S.; Pogue, B. W.; Hasan, T. Imaging and Photodynamic Therapy: Mechanisms, Monitoring, and Optimization. *Chem.*

Rev. **2010**, *110*, 2795-2838.

(17) Chen, H. C.; Tian, J. W.; He, W.J.; Guo. Z. J. H2O2-Activatable and O2-Evolving Nanoparticles for Highly Efficient and Selective Photodynamic Therapy against Hypoxic Tumor Cells. *J. Am. Chem. Soc.* **2015**, *137*, 1539-1547.

(18) Kim, H. M.; Cho, B. R. Small-molecule two-photon probes for bioimaging applications. *Chem. Rev.* **2015**, *115*, 5014-5055.

(19) Zheng, Z.; Zhang, T. F.; Liu, H. X.; Chen, Y. C.; Kwok, R. T. K.; Ma, C.; Zhang, P. F.; Sung, H. H. Y.; Williams, I. D.; Lam, J. W. Y.; Wong, K. S.; Tang, B. Z. Bright Near-Infrared Aggregation-Induced Emission Luminogens with Strong Two-Photon Absorption, Excellent Organelle Specificity, and Efficient Photodynamic Therapy Potential. *ACS Nano* **2018**, *12*, 8145-8159.

(20) He, G. S.; Tan, L. S.; Zheng, Q.; Prasad, P. N. Multiphoton Absorbing Materials: Molecular Designs, Characterizations, and Applications. *Chem. Rev.* **2008**, *108*, 1245-1330.

(21) Pawlicki, M.; Collins, H. A.; Denning, R. G.; Anderson, H. L. Two-Photon Absorption and the Design of Two-Photon Dyes. *Angew. Chem. Int. Ed.* **2009**, *48*, 3244-3266.

(22) Luo, J.; Xie, Z.; Lam, J. W.; Cheng, L.; Chen, H.; Qiu, C.; Kwok, H. S.; Zhan, X.; Liu, Y.; Zhu, D.; et al. Aggregation-Induced Emission of 1-methyl-1,2,3,4,5-pentapheylsilole. *Chem. Commun.* **2001**, 1740-1741.

(23) Yu, Z.; Duan, Y.; Cheng, L.; Han, Z.; Zheng, Z.; Zhou, H.; Wu, J.; Tian, Y. Aggregation Induced Emission in the Rotatable Molecules: the Essential Role of Molecular Interaction. *J. Mater. Chem*. **2012**, *22*, 16927-16932.

(24) Mei, J.; Leung, N. L.; Kwok, R. T.; Lam, J. W.; Tang, B. Z. Aggregation-Induced Emission: Together We Shine, United We Soar! *Chem. Rev.* **2015**, *115*, 11718-11940.

(25) Qin, W.; Li, K.; Feng, G.; Li, M.; Yang, Z.; Liu, B.; Tang, B. Z. Bright and photostable Organic Fluorescent Dots with Aggregation-Induced Emission Characteristics for Noninvasive Long-Term Cell Imaging. *Adv. Funct. Mater*. **2014**, *24*, 635-643.

(26) Zhao, E. G.; Chen, Y. L.; Wang, H.; Chen, S. J.; Lam, J. W. Y.; Leung, C. W. T.; Hong, Y. N.; Tang, B. Z. Light-enhanced bacterial killing and wash-free imaging based on AIE fluorogen. *ACS Appl. Mater. Inter*. **2015**, *7*, 7180-7188.

(27) Lin, G. W.; Manghnani, P. N.; Mao, D.; Thh, C.; Li, Y. H.; Zhao, Z. J.; Liu, B.; Tang, B. Z. Robust Red Organic Nanoparticles for In Vivo Fluorescence Imaging of Cancer Cell Progression in

Xenografted Zebrafish. *Adv. Funct. Mater.* **2017**, *27*, 1701418.

(28) Gao, M.; Su, H. F.; Lin, G. W.; Li, S. W.; Yu, X. S.; Qin, A. J.; Zhao, Z. J.; Zhang, Z. F.; Tang, B. Z. Targeted imaging of EGFR overexpressed cancer cells by brightly fluorescent nanoparticles conjugated with cetuximab. *Nanoscale* **2016**, *8*, 15027-15032.

(29) Geng J. L.; Li K.; Qin W.; Ma L.; Gurzadyan G. G.; Tang B. Z.; Liu B. Eccentric Loading of Fluorogen with Aggregation Induced Emission in PLGA Matrix Increases Nanoparticle Fluorescence Quantum Yield for Targeted Cellular Imaging. *Small* **2013**, *9*, 2012-2019.

(30) Makarov, N. S.; Drobizhev, M.; Rebane, A. Two-photon absorption standards in the 550-1600 nm excitation wavelength range. *Opt. Express* **2008**, *16*, 4029-4047.

(31) Wu, W. B.; Mao, D.; Hu, F.; Xu, S. D.; Chen, C.; Zhang C-J.; Cheng, X. M.; Yuan, Y. Y.; Ding, D.; Kong, D. L.; Liu, B. A Highly Efficient and Photostable Photosensitizer with Near-Infrared Aggregation-Induced Emission for Image-Guided Photodynamic Anticancer Therapy. *Adv. Mater.* **2017**, 29, 1700548.

(32) Wu, W. B.; Mao, D.; Xu, S. D.; Ji, S. L.; Hu, F.; Ding, D.; Kong, D. L.; B. Liu, High performance photosensitizers with aggregation-induced emission for image-guided photodynamic anticancer therapy. *Mater. Horiz.* **2017**, *4*, 1110-1114.

(33) Shi, X. J.; Sung, S. H. P.; Chau, J. H. C.; Li, Y.; Liu, Z. Y.; Kwok, R. T. K.; Liu, J. K.; Xiao, P. H.; Zhang, J. J.; Liu, B.; Lam, J. W. Y.; Tang, B. Z. Killing G(+) or G(−) Bacteria? The Important Role of Molecular Charge in AIE-Active Photosensitizers. *Small Methods* **2020**, 2000046.

(34) Neese, F. The ORCA program system. *WIREs Comput. Mol. Sci.* **2012**, *2*, 73-78.

(35) Neese, F. Software update: the ORCA program system, version 4.0. *WIREs Comput. Mol. Sci.* **2018**, *8,* DOI: 10.1002/wcms.1327.

(36) Wang, J. G.; Hou, Y. J.; Lei, W. H.; Zhou, Q. X.; Li, C.; Zhang, B. W.; Wang, X. S. DNA Photocleavage by a Cationic BODIPY Dye through Both Singlet Oxygen and Hydroxyl Radical: New Insight into the Photodynamic Mechanism of BODIPYs. *ChemPhysChem* **2012**, *13*, 2739-2747.

(37) Kumar, A.; Prasad, A.; Sedlarova, M.; Pospisil, P. Data on detection of singlet oxygen, hydroxyl radical and organic radical in Arabidopsis thaliana. *Data in Brief* **2018**, *21*, 2246-2252.

(38) Dewhirst, M. W.; Secomb, T. W.; Transport of drugs from blood vessels to tumour tissue. *Nat. Rev. Cancer* **2017**, *17*, 738-750.

1 (39) Weis, S. M.; Cheresh, D. A.; Tumor angiogenesis: molecular pathways and therapeutic targets.

2 *Nat. Med*. **2011**, *17*, 1359-1370.

3 (40) Li, X.; Li, H.; He, X. Z.; Chen, T.; Xia, X. Y.; Yang, C. X.; Zheng, W.; Spectrum- and time-

4 resolved endogenous multiphoton signals reveal quantitative differentiation of premalignant and

5 malignant gastric mucosa. *Biomed. Opt. Express*. **2018**, *9*, 453-471.

6 (41) Zipfel, W. R.; Williams, R. M.; Christie, R.; Nikitin, A. Y.; Hyman, B. T.; Webb, W. W. Live

7 tissue intrinsic emission microscopy using multiphoton-excited native fluorescence and second

8 harmonic generation. *P. Natl. Acad, Sci. U. S. A*. **2003**, *100*, 7075-7080.

9 (42) Qi, J.; Fang, Y.; Kwork, R. T. K.; Zhang, X. Y.; Hu, X. L.; Lam, J. W. Y.; Ding, D.; Tang, B. Z.

10 Highly Stable Organic Small Molecular Nanoparticles as an Advanced and Biocompatible

11 Phototheranostic Agent of Tumor in Living Mice. *ACS Nano* **2017**, *11*, 7177-7188.

12

13